

Fast entangling gates for Rydberg atoms via resonant dipole-dipole interaction

Giuliano Giudici,^{1,2,3} Stefano Veroni,³ Giacomo Giudice,³ Hannes Pichler,^{1,2} and Johannes Zeiher^{4,5,6}

¹*Institute for Theoretical Physics, University of Innsbruck, 6020 Innsbruck, Austria*

²*Institute for Quantum Optics and Quantum Information of the Austrian Academy of Sciences, 6020 Innsbruck, Austria*

³*PlanQC GmbH, Münchener Str. 34, 85748 Garching, Germany*

⁴*Fakultät für Physik, Ludwig-Maximilians-Universität München, 80799 Munich, Germany*

⁵*Max-Planck-Institut für Quantenoptik, 85748 Garching, Germany*

⁶*Munich Center for Quantum Science and Technology (MCQST), 80799 Munich, Germany*

The advent of digital neutral-atom quantum computers relies on the development of fast and robust protocols for high-fidelity quantum operations. In this work, we introduce a novel scheme for entangling gates using four atomic levels per atom: a ground state qubit and two Rydberg states. A laser field couples the qubit to one of the two Rydberg states, while a microwave field coupling the two Rydberg states enables a resonant dipole-dipole interaction between different atoms. We show that this interaction can mediate controlled-Z gates that are faster and less sensitive to Rydberg decay than state-of-the-art Rydberg gates based on van der Waals interactions. Moreover, we systematically stabilize our protocol against interatomic distance fluctuations and analyze its performance in realistic setups with rubidium or cesium atoms. Our results open up new avenues to the use of dipolar interactions for universal quantum computation with neutral atoms.

I. INTRODUCTION

The last decade has witnessed the rapid development of quantum platforms based on Rydberg atom arrays. In addition to their remarkable success as analog quantum simulators [1–4], neutral atoms trapped via optical tweezers or lattices are emerging as one of the most promising architectures for digital quantum computing, thanks to their scalability [5–7], their long coherence times [7–12], and their reconfigurable geometry that enables arbitrary qubit connectivity [8, 13]. High-fidelity single-qubit and two-qubit quantum operations have also been demonstrated with several atomic species, including rubidium [14, 15], cesium [16], strontium [17–20], and ytterbium [21–23]. Yet, further improving their accuracy remains one of the outstanding challenges toward realizing a large-scale, fault-tolerant quantum computer with neutral atoms, making it crucial to develop novel schemes for Rydberg gates.

Typically, two-qubit gates with Rydberg atoms rely on the strongly repulsive van der Waals force arising when the two atoms are in the same Rydberg state [15, 24–28]. The state-of-the-art approach for these schemes involves state-selectively coupling the atomic qubit of each atom to one Rydberg level via a laser, whose amplitude and phase are modulated in time to yield a controlled-Z (CZ) gate up to a local phase [25]. The phase and amplitude pulses required to achieve the desired two-qubit gate are not unique, providing a degree of freedom that can be exploited to minimize gate execution time [26] or maximize gate robustness against fluctuations in specific parameters [27, 29]. Time optimality is particularly relevant as the finite Rydberg lifetime is among the major sources of decoherence. Such protocols have been tested in a Rydberg array of rubidium atoms, achieving 99.5% gate fidelity [15], which is the most precise two-qubit quantum operation with neutral atoms to date.

Here, we present a different approach for realizing

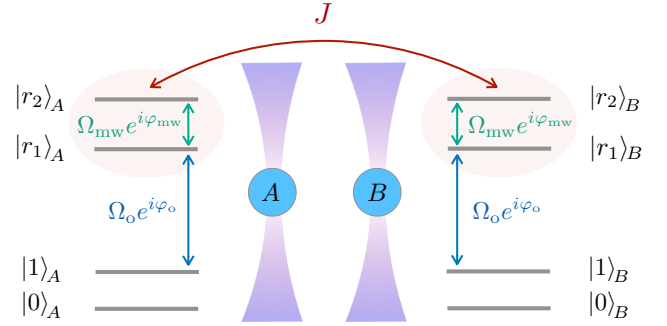


Figure 1. Schematic representation of the level scheme utilized in this work for realizing a CZ gate up to a local phase. A laser field with amplitude Ω_o and phase φ_o couples the qubit state $|1\rangle$ to the Rydberg state $|r_1\rangle$. A microwave field with amplitude Ω_{mw} and phase φ_{mw} couples the two Rydberg states $|r_1\rangle$ and $|r_2\rangle$ enabling a flip-flop interaction $J(|r_1r_2\rangle\langle r_2r_1| + \text{h.c.})$ between the two atoms (cf. Eq. (1)). Field amplitudes and phases are time-dependent control functions.

CZ Rydberg gates mediated by the resonant dipole-dipole interaction between pairs of distinct Rydberg levels $|r_1\rangle, |r_2\rangle$. Our scheme is depicted in Fig. 1: the atomic qubit state $|1\rangle$ is optically coupled to the Rydberg state $|r_1\rangle$, and $|r_1\rangle$ is microwave coupled to nearby Rydberg level $|r_2\rangle$, enabling a flip-flop interaction of strength J between the two atoms [30]. A similar setup was considered in Ref. [31] to construct adiabatic gate protocols. The laser field can be configured as either global, to enable parallel gate operations, or local, to target individual pairs of atoms. We use laser and microwave amplitudes Ω_o, Ω_{mw} and respective phases φ_o, φ_{mw} as time-dependent control functions, and apply the Gradient Ascent Pulse Engineering (GRAPE) method [32–36] to obtain the time-optimal protocol for this scheme. We show that the resulting gate is 20% faster than the time-optimal “van der Waals

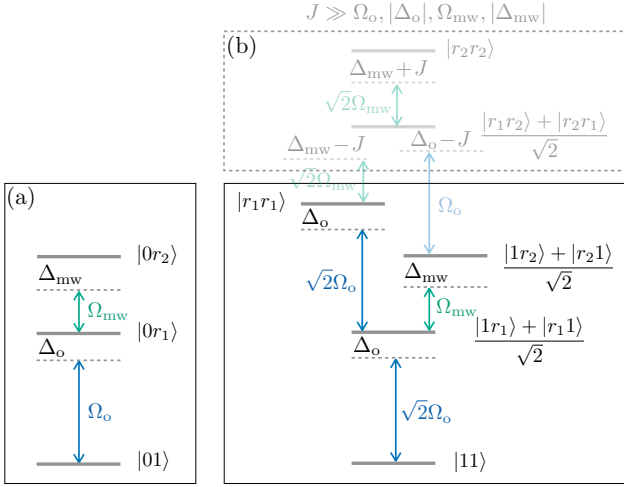


Figure 2. Schematic representation of the two relevant blocks of the Hamiltonian Eq. (1) that encode the dynamics of the state $|01\rangle$ (a) and $|11\rangle$ (b), after the unitary transformation $U = U_A \otimes U_B$, with $U_A = U_B = \text{diag}(1, e^{i\varphi_o}, e^{i(\varphi_o + \varphi_{mw})})$ mapping laser and microwave phases into detunings $\Delta_o = \frac{d\varphi_o}{dt}$, $\Delta_{mw} = \frac{d\varphi_{mw}}{dt}$. Because of the symmetry $A \leftrightarrow B$ of the protocol, all antisymmetric states are not relevant for the time evolution of $|11\rangle$. For $J \gg \Omega_o, |\Delta_o|, \Omega_{mw}, |\Delta_{mw}|$ the states in the shaded dashed box in panel (b) are decoupled from the dynamics of $|11\rangle$.

protocol” put forward in Ref. [26], and offers several other advantages such as reduced sensitivity to Rydberg decay, increased interaction strengths for long-range gates, and the possibility to combine optical addressability and global microwave control. We give a physical interpretation of the numerically obtained pulses in a regime where the dipole-dipole interaction strength J is much larger than all other energy scales, and find that the protocol can be formally interpreted as a reparametrization of the standard van der Waals protocol with time-dependent interaction strength. We then focus on realistic experimental conditions and develop a GRAPE-based method for further optimizing the pulse shapes to make the gate robust against fluctuations of the interaction strength J induced by the atomic motion. Finally, we perform numerical simulations that take atomic motion and finite Rydberg lifetimes into account for rubidium and cesium atoms and demonstrate Bell state fidelities that can exceed 99.9%, highlighting the feasibility and effectiveness of our scheme.

The structure of the paper is as follows. In Sec. II, we discuss two different protocols for realizing entangling gates with resonant dipole-dipole interactions between Rydberg atoms in the limit $J/\Omega_o \rightarrow \infty$. In particular, the first one consists of two resonant laser π -pulses with a fast microwave pulse at constant detuning in between; the second requires a time modulation of the laser and microwave detunings, and is mathematically equivalent to a van der Waals protocol with time-dependent interaction strength.

In Sec. III, we focus on the second protocol and lay out the numerical procedure employed to obtain the pulses that implement the CZ gate in the ideal case where no van der Waals interaction occurs between the Rydberg pair states. In Sec. IV, we consider rubidium and cesium atoms where the Rydberg states $|r_1\rangle$ and $|r_2\rangle$ are, respectively, P and S states with principal quantum numbers $n = 40, 50$. We compute their resonant dipole-dipole interaction strength J and van der Waals interaction strengths V_{11}, V_{12}, V_{22} at various distances, and repeat the GRAPE optimization to show that a qualitatively similar gate protocol exists in the presence of van der Waals forces. In Sec. V, we optimize the pulse robustness against fluctuations of the interatomic distance and find a stabilized protocol that significantly enhances gate fidelities when considering the coupling to the atomic motional state. In Sec. VI, we draw our conclusions and outline potential directions for future work.

II. CZ GATES FROM RESONANT DIPOLE-DIPOLE INTERACTION

The Hamiltonian that describes the two four-level systems depicted in Fig. 1 reads

$$\begin{aligned} \frac{H(t)}{\hbar} = & \frac{\Omega_o(t)}{2} \left(e^{i\varphi_o(t)} |1\rangle\langle r_1|_A + e^{i\varphi_o(t)} |1\rangle\langle r_1|_B + \text{h.c.} \right) \\ & + \frac{\Omega_{mw}(t)}{2} \left(e^{i\varphi_{mw}(t)} |r_1\rangle\langle r_2|_A + e^{i\varphi_{mw}(t)} |r_1\rangle\langle r_2|_B + \text{h.c.} \right) \\ & + J (|r_1r_2\rangle\langle r_2r_1| + \text{h.c.}), \end{aligned} \quad (1)$$

where A and B label the two atoms, Ω_o and φ_o are the amplitude and phase of the laser that couples the computational basis state $|1\rangle$ to the Rydberg state $|r_1\rangle$, Ω_{mw} and φ_{mw} are the amplitude and phase of the microwave radiation that couples the two Rydberg states $|r_1\rangle$ and $|r_2\rangle$, and $J > 0$ is the strength of the dipolar exchange interaction. Such interaction is present in Rydberg states for which a dipole transition is allowed, e.g. an s state and a p state (cf. Sec. IV). The real Hamiltonian for the two atoms also includes van der Waals interaction terms of the form $V_{ij} |r_i r_j\rangle\langle r_i r_j|$, which we will neglect in this section and discuss at length in Sec. IV and Sec. V.

The most general maximally-entangling two-qubit gate realizable within this scheme is a CZ gate up to a single-qubit phase shift, which can be parameterized by an angle θ and can be written in the computational basis $\{|00\rangle, |01\rangle, |10\rangle, |11\rangle\}$ as

$$\text{CZ}(\theta) = \text{diag}(1, e^{i\theta}, e^{i\theta}, -e^{i2\theta}). \quad (2)$$

We now outline two ways for obtaining such two-qubit gate from the dynamics Eq. (1) when $J \gg \Omega_o, |\Delta_o|, \Omega_{mw}, |\Delta_{mw}|$, where $\Delta_o = \frac{d\varphi_o}{dt}$ and $\Delta_{mw} = \frac{d\varphi_{mw}}{dt}$. We postpone the discussion of gate protocols at finite J to Sec. III B. In what follows, we switch to a description in terms of the detunings Δ_o (Δ_{mw}) with re-

spect to the optical (microwave) transition, by applying the unitary transformation $U = U_A \otimes U_B$, where $U_A = U_B = \text{diag}(1, 1, e^{i\varphi_o}, e^{i(\varphi_o + \varphi_{mw})})$. The time evolution of $|01\rangle$ (or $|10\rangle$) and $|11\rangle$ is governed by the Hamiltonians H_{01} and H_{11} depicted in Fig. 2. The flip-flop interaction only enters in H_{11} and, for $J \gg \Omega_o, |\Delta_o|, \Omega_{mw}, |\Delta_{mw}|$, results in the states $\frac{1}{2}(|r_1 r_2\rangle + |r_2 r_1\rangle)$ and $|r_2 r_2\rangle$ being far off-resonant and effectively decoupled from the dynamics.

A simple protocol for realizing a CZ(θ) gate in this limit consists of three steps. First a resonant optical π -pulse transfers the single qubit population from $|1\rangle$ to $|r_1\rangle$, such that

$$U_1 |01\rangle = -i |0r_1\rangle, \quad U_1 |11\rangle = -|r_1 r_1\rangle. \quad (3)$$

A second off-resonant microwave pulse U_2 at constant detuning Δ_{mw} is then applied to the atoms. Since the laser is off during this pulse, the state $|r_1 r_1\rangle$ does not evolve under U_2 (cf. Fig. 2). Hence, one can choose a pulse duration $T_{mw} = 2\pi/\sqrt{\Delta_{mw}^2 + \Omega_{mw}^2}$ such that $|0r_1\rangle$ undergoes a complete Rabi oscillation $U_2 |0r_1\rangle = e^{i\varphi_{mw}} |0r_1\rangle$, acquiring a phase $\pi(1 + \Delta_{mw}/\sqrt{\Delta_{mw}^2 + \Omega_{mw}^2})$ that can be adjusted by tuning Δ_{mw} . Setting $\Delta_{mw} = \mp\Omega_{mw}/\sqrt{3}$ yields $\varphi_{mw} = \pm\pi/2$ and $\Omega_{mw}T_{mw} = \sqrt{3}\pi$. The combined result for these two pulses is

$$U_2 U_1 |01\rangle = -ie^{\pm i\frac{\pi}{2}} |0r_1\rangle, \quad U_2 U_1 |11\rangle = -|r_1 r_1\rangle. \quad (4)$$

Finally, a resonant optical π -pulse U_3 is applied to bring back the population to the computational basis:

$$U_3 U_2 U_1 |01\rangle = -e^{\pm i\frac{\pi}{2}} |0r_1\rangle, \quad U_3 U_2 U_1 |11\rangle = |r_1 r_1\rangle. \quad (5)$$

By comparing with Eq. (2), one can see that this pulse sequence realizes a CZ($\pm 3\pi/2$) gate in a time

$$\Omega_o T = 2\pi + \frac{\sqrt{3}\pi\Omega_o}{\Omega_{mw}}. \quad (6)$$

As we discuss in App. A, when $\Omega_{mw} \gg \Omega_o$, the microwave pulse U_2 is much faster than the two laser pulses U_1 and U_3 and can be executed without turning off the laser with negligible effect on the gate fidelity. This condition is easily achievable with standard microwave sources [37]. Moreover, a proper time-modulation of the microwave phase can accommodate a finite dipole-dipole interaction strength J . However, we could not find a straightforward extension of this protocol that is stable upon the inclusion of van der Waals interactions V_{ij} .

A natural question that emerges at this point is whether both optical and microwave couplings can be used at the same time to find an improved gate protocol. In the following, we present such a protocol and show that it can be systematically adapted to the case where van der Waals interactions are present and will be the focus of the rest of the main text. We describe below its simplest version when $J \gg \Omega_o, |\Delta_o|, \Omega_{mw}, |\Delta_{mw}|$ and give its physical interpretation. We assume laser and microwave fields to be always on with constant amplitudes Ω_o and Ω_{mw} , and

consider the microwave detuning $\Delta_{mw} \gg \Omega_o, \Delta_o, \Omega_{mw}$. In this limit the dynamics of $|01\rangle$ depicted in Fig. 2 can be further restricted to only two levels. To see this, we diagonalize H_{01} in the subspace $\{|0r_1\rangle, |0r_2\rangle\}$ at first order in $\lambda = \Omega_{mw}/2\Delta_{mw}$. H_{01} expressed in the dressed basis $\{|01\rangle, |0r_1\rangle + \lambda|0r_2\rangle, |0r_2\rangle - \lambda|0r_1\rangle\}$ reads

$$\frac{H_{01}}{\hbar} = \begin{pmatrix} 0 & \frac{\Omega_o}{2} & -\frac{\Omega_{mw}\Omega_o}{4\Delta_{mw}} \\ \frac{\Omega_o}{2} & -\Delta_o + \frac{\Omega_{mw}^2}{4\Delta_{mw}} & 0 \\ -\frac{\Omega_{mw}\Omega_o}{4\Delta_{mw}} & 0 & -\Delta_o - \Delta_{mw} - \frac{\Omega_{mw}^2}{4\Delta_{mw}} \end{pmatrix}. \quad (7)$$

The AC Stark shift induced on the dressed states $|0r_1\rangle + \lambda|0r_2\rangle$ and $|0r_2\rangle - \lambda|0r_1\rangle$ can be made finite by setting $\Delta_{mw} = \tau\Omega_{mw}^2$. If we now assume $\Omega_{mw} \gg \Omega_o, \Delta_o$ the state $|0r_2\rangle$ decouples from the dynamics of $|01\rangle$, which is governed by the two-level Hamiltonian

$$\frac{H_{01}}{\hbar} = \begin{pmatrix} 0 & \frac{\Omega_o}{2} \\ \frac{\Omega_o}{2} & -\Delta_o + \frac{1}{4\tau} \end{pmatrix}. \quad (8)$$

The same argument can be applied to H_{11} upon replacing $\{|0r_1\rangle, |0r_2\rangle\}$ with $\{\frac{1}{\sqrt{2}}(|1r_1\rangle + |r_1 1\rangle), \frac{1}{\sqrt{2}}(|1r_2\rangle + |r_2 1\rangle)\}$. In the basis $\{|11\rangle, \frac{1}{\sqrt{2}}(|1r_1\rangle + |r_1 1\rangle), |r_1 r_1\rangle\}$ the resulting three-level Hamiltonian is

$$\frac{H_{11}}{\hbar} = \begin{pmatrix} 0 & \frac{\Omega_o}{\sqrt{2}} & 0 \\ \frac{\Omega_o}{\sqrt{2}} & -\Delta_o + \frac{1}{4\tau} & \frac{\Omega_o}{\sqrt{2}} \\ 0 & \frac{\Omega_o}{\sqrt{2}} & -2\Delta_o \end{pmatrix}. \quad (9)$$

The dynamics described by Eq. (8) and Eq. (9) is mathematically equivalent to the one of two three-level systems $\{|0\rangle, |1\rangle, |r\rangle\}$, where the state $|rr\rangle$ interacts with van der Waals force $V = -1/(2\tau)$, and where the detuning from the Rydberg transition is given by $\Delta = \Delta_o - 1/(4\tau)$, i.e. the two-qubit gate scheme of Refs. [25]. The Hamiltonian for this system is

$$\begin{aligned} \frac{H(t)}{\hbar} = & \frac{\Omega_o}{2} (|1\rangle\langle r|_A + |1\rangle\langle r|_B + \text{h.c.}) \\ & - \Delta(t) (|r\rangle\langle r|_A + |r\rangle\langle r|_B) + V(t) |rr\rangle\langle rr|. \end{aligned} \quad (10)$$

In the prototypical van der Waals gate, the distance between the atoms and thus the van der Waals coefficient V are usually constant during the gate operation. In our scheme, instead, a time-dependent V simply corresponds to a time modulation of the microwave detuning Δ_{mw} . We will show in the next section that this additional control function provides a substantial speedup w.r.t. constant- V van der Waals gates. In particular, we will demonstrate that the shortest gate time for a CZ operation with the Hamiltonian Eq. (10) is $T \simeq 5.98/\Omega_o$, compared to the van der Waals gates execution time of $T \simeq 7/\Omega_o$ for $V/\Omega_o \simeq 1.3$ (see App. B) and $T \simeq 7.6/\Omega_o$ for $V/\Omega_o = \infty$ [26]. We will also show that the obtained protocol can be extended to finite Ω_{mw}/Ω_o and J/Ω_o with a slight increase of the gate execution time. We further observe that a time modulation of both Δ and V in Eq. (10)

is achieved via a time-dependent microwave detuning Δ_{mw} , since $\tau = \Delta_{\text{mw}}/\Omega_{\text{mw}}^2$, potentially simplifying the hardware requirements for realizing two-qubit gates within the scheme presented in this work.

III. GATE SPEED OPTIMIZATION

In this section, we employ GRAPE to find the time-optimal protocol that realizes a CZ(θ) gate Eq. (2) within the scheme of Fig. 1. This gate maps the product state $|++\rangle$ to the Bell state

$$|\psi_\theta\rangle = \frac{1}{2} (|00\rangle + e^{i\theta} |01\rangle + e^{i\theta} |10\rangle - e^{2i\theta} |11\rangle), \quad (11)$$

such that the Bell state fidelity

$$F_{\text{Bell}} = \left| \langle \psi_\theta | \mathcal{T} \exp \left(-\frac{i}{\hbar} \int_0^T H(t) dt \right) | ++ \rangle \right|^2 = 1, \quad (12)$$

where $\mathcal{T} \exp$ is the time-ordered exponential. This quantity has been often used to benchmark and optimize the CZ gate [25, 38–40]. Since such gate is diagonal, $F_{\text{Bell}} = 1$ is equivalent to $F = 1$, where F is the average gate fidelity [41]. We use the Bell state infidelity $\mathcal{C} = 1 - F_{\text{Bell}}$ as a cost function for the optimization, discretize time with a time step dt , and numerically minimize the cost function \mathcal{C} for a fixed total time T . The number of variational parameters for $dt = T/N$ is $kN + 1$, where k is the number of control functions and N is the number of time steps. Such parameters are the values $f_i = f(t_i)$ of the unknown functions f computed on the time-grid $t_i = (i + \frac{1}{2})dt$, $i = 0, \dots, N - 1$, and the Bell state angle θ . We will always keep a constant laser amplitude Ω_o , which fixes our time units, and use $\varphi_o(t), \varphi_{\text{mw}}(t)$ as control functions for $J/\Omega_o = \infty$ and $\varphi_o(t), \varphi_{\text{mw}}(t), \Omega_{\text{mw}}(t)$ for finite J/Ω_o . We repeat the optimization for increasing T until a time T^* is found for which the cost function \mathcal{C} vanishes. The numerical minimization is performed using the method “L-BFGS-B” as implemented in the Python library SciPy [42]. To speed up this procedure we provide the SciPy routine with the gradient of the (time-discrete) cost function, which can be straightforwardly computed analytically. Moreover, when the microwave amplitude Ω_{mw} is also used as a variational control function, we set a lower bound $\Omega_{\text{mw}}^{\text{min}} = 0$ to ensure its positivity.

In the remainder of this section we employ GRAPE to first show that the scheme of Fig. 1, in the double limit $J/\Omega_o \rightarrow \infty$ and $\Omega_{\text{mw}}/\Omega_o \rightarrow \infty$ with $\Delta_{\text{mw}} = \tau\Omega_{\text{mw}}^2$, enables the realization of an exact CZ(θ) gate in a time $T \simeq 5.98/\Omega_o$. We then apply a modified version of the same method to find the time-optimal CZ gate protocol attainable with the Hamiltonian Eq. (1) and a finite dipole-dipole interaction strength J .

A. Infinite J/Ω_o

In Sec. II, we proved that the system of two dipole-dipole interacting four-level atoms depicted in Fig. 1 could be mapped to a system of two three-level atoms interacting via a time-dependent van der Waals force $V(t)$ and Rydberg-transition detuning $\Delta(t)$. This mapping is valid in the limits $J/\Omega_o \rightarrow \infty$ and $\Omega_{\text{mw}}/\Omega_o \rightarrow \infty$ with $\Delta_{\text{mw}} = \tau\Omega_{\text{mw}}^2$, and the relations between the parameters of the two models are $V(t) = -1/(2\tau(t))$ and $\Delta(t) = \Delta_o(t) - 1/(4\tau(t))$. We now perform a GRAPE optimization on the Hamiltonian Eq. (10) using the $\Delta(t)$, $V(t)$, and the CZ gate angle θ (cf. Eq. (2)) as variational parameters. The results of this optimization for $N = 100$ time steps are the solid black lines in Fig. 3. In Fig. 3(a), we plot the Bell state infidelity as a function of the dimensionless gate time $\Omega_o T$. The infidelity sharply drops to zero (within numerical precision) at the minimum time T^* for which an exact CZ gate is realized, demonstrating the existence, under ideal conditions, of an exact CZ(θ) gate in a time $T \simeq 5.98/\Omega_o$. In Figs. 3(c) and 3(d), we plot the time dependence of the functions $f_1 = \Delta - V/2$ and $f_2 = -2V$ respectively for $\Omega_o T = 5.9$. These two functions have a direct interpretation in the dipole-dipole interacting gate scheme of Fig. 1, with $f_1 = \frac{d\varphi_o}{dt}$ and $f_2 = \Omega_{\text{mw}}^2 / \frac{d\varphi_{\text{mw}}}{dt}$.

Although this correspondence only holds when $\Omega_{\text{mw}}/\Omega_o = \infty$, GRAPE remarkably finds a qualitatively similar solution for finite $\Omega_{\text{mw}}/\Omega_o$. To show this, we minimize the Bell state infidelity obtained by evolving $|++\rangle$ with the Hamiltonian Eq. (1), using the laser and microwave phases $\varphi_o(t)$ and $\varphi_{\text{mw}}(t)$ as variational control functions. We enforce the constraint $J/\Omega_o = \infty$ by projecting out the states $|r_1 r_2\rangle, |r_2 r_1\rangle, |r_2 r_2\rangle$ from the dynamics (cf. Fig. 2(b)). We plot in Fig. 3(a) the minimum infidelity as a function of $\Omega_o T$ for different values of $\Omega_{\text{mw}}/\Omega_o$, and in Figs. 3(c) and 3(d) the functions $f_1 = \frac{d\varphi_o}{dt}$ and $f_2 = \Omega_{\text{mw}}^2 / \frac{d\varphi_{\text{mw}}}{dt}$ for $\Omega_o T = 5.9$, where $\frac{d}{dt}$ denotes a numerical derivative taken for a time step T/N with $N = 300, 600$. We compare this result to the one obtained from the Hamiltonian Eq. (10) and observe a rapid convergence to the limit $\Omega_{\text{mw}}/\Omega_o = \infty$.

The finite- Ω_{mw} pulse depicted in Fig. 3(d) is discontinuous at $t/T \simeq 0.25, 0.75$. This is because the optimal $V(t) \propto 1/\frac{d\varphi_{\text{mw}}}{dt}$ vanishes, causing divergences in the optimal $\varphi_{\text{mw}}(t)$ and slow convergence of the result with the number of time steps N (cf. Fig. 3(b)). Although this discontinuity in $1/\varphi_{\text{mw}}$ can be made arbitrarily small by reducing the time step $dt = T/N$, for too large N the numerical optimization becomes unstable and eventually fails to produce a continuous solution. This issue is even more severe when the constraint $J/\Omega_o = \infty$ is relaxed. For this reason, for the GRAPE optimization at finite J/Ω_o below we introduce a regularizer in the cost function that penalizes discontinuous solutions.

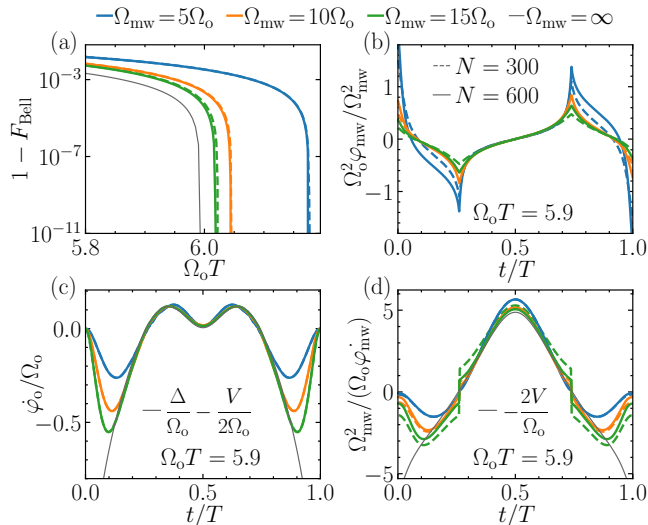


Figure 3. (a) Bell state infidelity as a function of the dimensionless gate time $\Omega_o T$ obtained for the Hamiltonian Eq. (10) (black lines) and for the Hamiltonian Eq. (1) with $J/\Omega_o = \infty$ for different values of Ω_{mw}/Ω_o (colored lines). In the latter case, the optimization is performed for two different time step sizes $dt = T/N$, i.e. $N = 300$ (dashed lines) and $N = 600$ (solid lines), while in the former case $N = 100$. (b) Optimal microwave phase obtained at finite Ω_{mw} for different values of Ω_{mw}/Ω_o and for $\Omega_o T = 5.9$. (c)–(d) Comparison between the pulse shapes obtained for the Hamiltonian Eq. (10) (black lines) and for the Hamiltonian Eq. (1) with $J/\Omega_o = \infty$ (colored lines). The relations between the parameters of the two models are $\dot{\varphi}_o \equiv \frac{d\varphi_o}{dt} = \Delta - V/2$, $\dot{\varphi}_{mw} \equiv \frac{d\varphi_{mw}}{dt} = -\Omega_{mw}^2/(2V)$, and imply that φ_{mw} diverges when V vanishes (cf. panel (b)).

B. Finite J/Ω_o

For the GRAPE optimization of the CZ gate protocol implemented via the Hamiltonian Eq. (1) we use the control functions $\varphi_o(t)$, $\varphi_{mw}(t)$, $\Omega_{mw}(t)$. As previously discussed in Sec. III A, this procedure is numerically unstable due to divergences in the optimal microwave phase φ_{mw} and yields optimal pulses that do not converge to smooth curves with increasing N (decreasing time step dt). To overcome this issue we add a regularizer to the cost function that penalizes discontinuous solutions:

$$\begin{aligned} \mathcal{C}_\eta &= 1 - F_{\text{Bell}} + \eta \sum_f \int_0^T \left(\frac{df}{dt} \right)^2 dt \\ &\simeq 1 - F_{\text{Bell}} + \eta \frac{N}{T} \sum_f \sum_{i=0}^{N-1} (f_{i+1} - f_i)^2, \end{aligned} \quad (13)$$

where $f = \varphi_o, \varphi_{mw}, \Omega_{mw}$ and η is a small constant that we adjust as the exact gate at time T^* is approached. Specifically, we initially set $\eta_0 = 10^{-7}$ for $T_0 < T^*$ and carry out the optimization until convergence. We then use the resulting optimal pulses as initial conditions for the optimization at $T_1 = T_0 + dT$, with $dT = 0.002/\Omega_o$,

and reset $\eta_1 = \varepsilon \mathcal{C}_0$, where \mathcal{C}_0 is the Bell state infidelity obtained for the optimal solution at time T_0 . By iterating this procedure we systematically reduce η as T^* is approached. We empirically find that the control functions obtained in this way are smooth and independent of the time step, as long as $\varepsilon \geq 10^{-3}$. Increasing ε results in a larger T^* . Therefore, we tune ε to the minimum value for which the optimal pulses are independent of the discretization scale dt .

The resulting pulses are plotted in Fig. 4 for several values of J/Ω_o and $N = 200$. In Fig. 4(a) we show the Bell state infidelity as a function of the total time T . The minimum gate execution time T^* is J -dependent and decreases with increasing J/Ω_o . As plotted in Fig. 5(a), it ranges from $T^* \simeq 6.28/\Omega_o$ for $J/\Omega_o = 10$ to $T^* \simeq 6.09/\Omega_o$ for $J/\Omega_o = 50$.

Figure 5(a) also displays the relative speed-up with respect to the execution time $T_V^* \simeq 7.61/\Omega_o$ of the time-optimal van der Waals gate [26], which goes from 18% up to 20% for $J/\Omega_o = 10$ and 50, respectively. We observe that the divergences in the microwave phase φ_{mw} reported in Fig. 3(b) become smooth peaks in Fig. 4(c) at times $t/T \simeq 0.25, 0.75$ due to the regularizer.

Another important quantity to monitor is the time spent in the Rydberg manifold during the protocol, as it upper-bounds the infidelity due to the finite lifetime of the Rydberg states. It is given by

$$T^R = \frac{1}{2^2} \sum_q \int_0^T \langle q(t) | (\Pi_A + \Pi_B) | q(t) \rangle dt, \quad (14)$$

where $\Pi = |r_1\rangle\langle r_1| + |r_2\rangle\langle r_2|$ is the projector on the Rydberg subspace of one atom, the sum runs on all the computational basis states $|q\rangle = \{|00\rangle, |01\rangle, |10\rangle, |11\rangle\}$, and $|q(t)\rangle$ is the time evolution of these states under the optimal protocol. We plot $\Omega_o T^R$ vs J/Ω_o in Fig. 5(b), demonstrating another substantial improvement ranging from 22% to 26% for $J/\Omega_o = 10$ and 50 with respect to the van der Waals gate $T_V^R \simeq 2.95/\Omega_o$ [26].

IV. IMPLEMENTATION WITH ALKALI ATOMS

So far, we neglected the van der Waals interactions arising when the two atoms are in a Rydberg state. Such interactions take the form

$$H_{\text{vdW}} = \sum_{i,j=1}^2 V_{ij} |r_i r_j\rangle\langle r_i r_j| \quad (15)$$

and have to be included in the Hamiltonian Eq. (1). We do not expect the gate protocols depicted in Fig. 3 to be sensitive to the value of the interaction strengths $V_{12} (= V_{21}), V_{22}$. In fact, $J \gg \Omega_o$ and $|V_{12}|, |V_{22}| \gg \Omega_o$ have the same effect on the state $|11\rangle$, decoupling the states $|r_1 r_2\rangle, |r_2 r_2\rangle$ from its dynamics. On the contrary, $|V_{11}|$ has to be much smaller than Ω_o to avoid the decoupling of $|r_1 r_1\rangle$, which plays an active role in our scheme, as

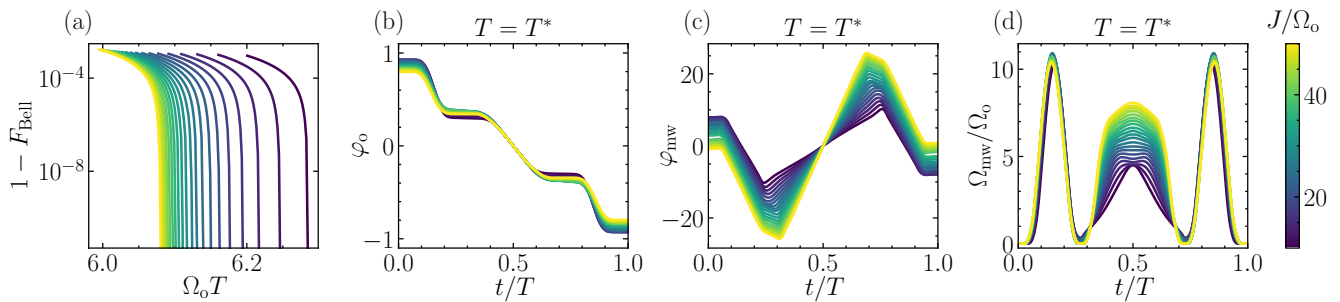


Figure 4. (a) Bell state infidelity as a function of the dimensionless gate time $\Omega_o T$ for several values of J/Ω_o ranging between 10 and 50 (cf. colorbar on the right of panel (d)). The number of time steps is set to $N = 200$ and the regularizing parameter $\varepsilon = 10^{-3}$ (cf. Eq. (13) and the text below). (b)–(d) Optimal laser phase φ_o , microwave phase φ_{mw} and microwave amplitude Ω_{mw} at the time T^* for which the time-optimal exact gate is found by the GRAPE optimization.

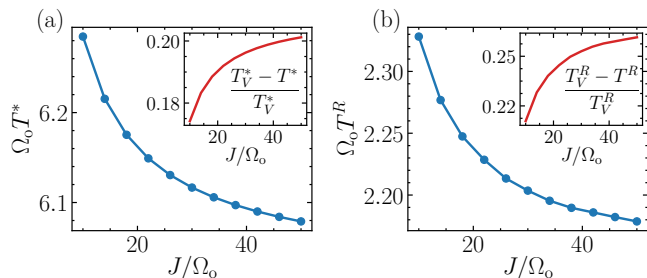


Figure 5. (a) Optimal CZ gate execution time for the pulses shown in Fig. 4 as a function of J/Ω_o (blue markers). The inset shows the relative speed-up $(T_V^* - T^*)/T_V^*$ w.r.t. the time-optimal van der Waals gate of Ref. [26] for which $\Omega_o T_V^* \simeq 7.61$ (red line). (b) Same as (a) with the time spent in the Rydberg subspace T^R Eq. (14) in place of the gate execution time T^* .

we discussed in Sec. III. Finally, we need to have $J \gg \Omega_o$ since the execution time of our protocol decreases with increasing J/Ω_o (cf. Fig. 5(a)). Combining these requirements we have the condition $J \gg \Omega_o \gg |V_{11}|$.

The interactions strengths J and V_{11} depend on the interatomic distance R as $J(R) \sim C_3/R^3$ and $V_{11}(R) \sim C_6/R^6$, respectively. Hence, we can adjust $J/V_{11} \sim (C_3/C_6)R^3$ by tuning R . However, Ω_o has to be as large as possible since the real gate time $T \propto 1/\Omega_o$. The maximum optical Rabi frequencies achievable in typical experimental conditions $\Omega_o/2\pi \simeq 1 - 10$ MHz thus set the range of the required dipole-dipole and van der Waals interactions to $J/2\pi \simeq 10 - 100$ MHz and $V/2\pi \simeq 0.1 - 1$ MHz. The C_3 and C_6 coefficients depend on the atomic species and the quantum numbers of the Rydberg states. Their scaling with the principal quantum number n is $C_3 \sim n^4$ and $C_6 \sim n^{11}$ [43]. Therefore, $J/|V_{11}|$ decreases with n for fixed R . Given the Rydberg lifetime scaling $\tau \sim n^2$ at room temperature, we need to find a tradeoff between large $J/|V_{11}|$ and long τ . Below, we focus on rubidium and cesium atoms with $n = 40$ and $n = 50$, which are among the most used atomic species in Rydberg atom experiments [8, 10, 44, 45]. In particular, we choose $|r_1\rangle = |nP_{3/2}, m_J = 3/2\rangle$ and $|r_2\rangle = |nS_{1/2}, m_J = 1/2\rangle$.

Rb					
n	R (μm)	$J/2\pi$ (MHz)	V_{11}/J	V_{12}/J	V_{22}/J
40	2.51	50	0.007	0.008	0.079
40	2.45	70	0.010	0.011	0.110
50	3.45	50	0.015	0.020	0.182
50	2.83	70	0.020	0.028	0.255

Cs					
n	R (μm)	$J/2\pi$ (MHz)	V_{11}/J	V_{12}/J	V_{22}/J
40	2.43	50	-0.011	0.007	0.064
40	2.17	70	-0.015	0.010	0.089
50	3.36	50	-0.022	0.019	0.150
50	3.00	70	-0.030	0.026	0.210

Table I. Resonant dipole-dipole and van der Waals interaction strengths J and V_{ij} between pairs of rubidium and cesium Rydberg states $|r_1\rangle = |nP_{3/2}, m_J = 3/2\rangle$ and $|r_2\rangle = |nS_{1/2}, m_J = 1/2\rangle$ with $n = 40$ and $n = 50$ at a distance R .

This choice is motivated by the fact that the C_6 coefficient is smaller for P states than for S states. We calculate the interaction strengths J, V_{ij} using the Python package PAIRINTERACTION [46]. Selected results that will be employed in what follows are reported in Table I. We note that $V_{11} < 0$ for cesium, a feature that makes the gate more robust against fluctuations in R , as we will show in Sec. V (cf. Fig. 6(a)).

We carried out the GRAPE optimization outlined in Sec. III B including the van der Waals interaction Eq. (15) in the Hamiltonian Eq. (1), with laser phase, and microwave amplitude and phase as control functions. We set $8 \leq J/\Omega_o \leq 14$ and the V_{ij} listed in Table I. These interaction strengths enable Rabi frequencies $\Omega_o/2\pi \simeq 3.6 - 6.3$ MHz for $J/2\pi = 50$ MHz and $\Omega_o/2\pi \simeq 5 - 8.75$ MHz for $J/2\pi = 70$ MHz. The time-optimal pulses resulting from this procedure are similar to the ones depicted in Fig. 4 and yield almost the same

gate time. One example obtained for $J/\Omega_o = 10$ and the interaction strengths in the first row of Table I for rubidium Rydberg states is the dark grey line in Fig. 6.

V. GATE ROBUSTNESS OPTIMIZATION

The main drawback of the experimentally realizable gate protocols of Sec. IV lies in the fact that the finite value of J/Ω_o and the inclusion of small but non-negligible van der Waals forces make them sensitive to fluctuations δR of the interatomic distance, which induce variations of the interaction strengths $\delta J/J = -3\delta R/R$ and $\delta V/V = -6\delta R/R$. The same issue arises with standard van der Waals protocols away from the blockade regime. To overcome this limitation we employ a simple cost function for GRAPE that targets pulse shapes more stable against small changes of R . Upon defining $x = \delta R/R$, such cost function has the form [47]

$$\mathcal{C} = 1 - \frac{1}{2x_M} \int_{-x_M}^{x_M} dx F_{\text{Bell}}(x), \quad (16)$$

where $x_M = \delta R_M/R$ is the maximum fluctuation and $F_{\text{Bell}}(x)$ is the Bell state fidelity corresponding to a Hamiltonian with $J \cdot (1 - 3x)$ and $V_{ij} \cdot (1 - 6x)$.

For the numerical optimization, we discretize the integral in Eq. (16) on K points and include the regularizer in Eq. (13) to ensure the smoothness of the optimal control functions. We use the time-optimal pulses obtained for a given set of parameters J, V_{ij} as the initial condition for the optimization and allow for a slight increase of the gate time $T = T^* + \delta T^*$, where T^* is the minimal time for realizing an exact CZ(θ) gate (cf. Fig. 4). Remarkably, we find that the resulting optimal pulses are independent of x_M provided that K is large enough. In practice, we set $x_M = 0.033$ and $K = 11$, and observe that increasing x_M and K yields the same pulses at a larger computational cost. The result is depicted in Fig. 6 for the set of interaction strengths J, V_{ij} in the first row of Table I for rubidium (top) and cesium (bottom) Rydberg states. While the stabilized pulses (colored lines) are qualitatively similar to the time-optimal exact protocol (dark grey lines), their Bell state infidelity in Fig. 6(a) is one order of magnitude smaller over the whole interval $|\delta R/R| \leq 0.033$, excluding a small neighborhood of $\delta R/R = 0$. We notice that stabilized pulses for cesium produce smaller infidelities for a larger range of $\delta R/R$, indicating that the attractive van der Waals interaction is beneficial for the gate stabilization (cf. bottom and top of Fig. 6(a)). The result significantly improves when a small increase in the gate time δT^* is allowed.

A. Gate performance with atomic motion

To benchmark the performance of the robust pulses such as those shown in Fig. 6, we carried out numerical

simulations including the spontaneous Rydberg decay and the atomic motion induced by thermal fluctuations and photon recoil. For the case of a single-photon Rydberg transition considered below, photon recoil accounts for most of the gate infidelity if laser phase and amplitude noise are negligible [48]. For a two-photon transition, instead, the recoil can be suppressed by using counter-propagation beams. However, this introduces scattering from the intermediate state, which remains a major source of gate infidelity, which can be partly mitigated via pulse modulation [15]. We assume that the initial motional state is a thermal state $\rho \propto \exp(-\beta \hbar \omega_{\text{trap}} \sum_{\ell=A,B} a_{\ell}^{\dagger} a_{\ell})$, where ω_{trap} is the trap frequency and a (a^{\dagger}) are the annihilation (creation) operators of the motional modes. The tweezer traps are turned off during the gate, such that the vibrational modes' Hamiltonian reads

$$H_{\text{motion}} = \sum_{\ell=A,B} \frac{P_{\ell}^2}{2m}, \quad (17)$$

where $P_{\ell} = ip_{\text{osc}}(a_A^{\dagger} - a_A)$, $p_{\text{osc}} = \sqrt{\hbar m \omega_{\text{trap}}/2}$, and m is the atomic mass. The full model Hamiltonian is $H = H_{\text{motion}} + H_{\text{atom}} + H_{\text{int}} + H_{\text{decay}}$. The second term is the Hamiltonian of the atomic levels including the momentum transfer of the laser and microwave fields:

$$\begin{aligned} \frac{H_{\text{atom}}}{\hbar} &= \frac{\Omega_o}{2} \sum_{\ell=A,B} \left(e^{i\varphi_o + i\eta_o(a_{\ell} + a_{\ell}^{\dagger})} |1\rangle\langle r_1|_{\ell} + \text{h.c.} \right) + \\ &+ \frac{\Omega_{\text{mw}}}{2} \sum_{\ell=A,B} \left(e^{i\varphi_{\text{mw}} + i\eta_{\text{mw}}(a_{\ell} + a_{\ell}^{\dagger})} |r_1\rangle\langle r_2|_{\ell} + \text{h.c.} \right), \end{aligned} \quad (18)$$

where $\eta_o = 2\pi x_{\text{osc}}/\lambda_o$ and $\eta_{\text{mw}} = 2\pi x_{\text{osc}}/\lambda_{\text{mw}}$ are the Lamb Dicke parameters for the optical and microwave transitions, with $x_{\text{osc}} = \sqrt{\hbar/(2m\omega_{\text{trap}})}$ and $\lambda_o(\lambda_{\text{mw}})$ the optical (microwave) transition wavelength. The third term is the interaction Hamiltonian where the dipole-dipole and van der Waals potentials are expanded at first order in the interatomic distance fluctuations $\Delta_{\text{mw}}R = X_A - X_B = x_{\text{osc}}(a_A + a_A^{\dagger} - a_B - a_B^{\dagger})$:

$$\begin{aligned} \frac{H_{\text{int}}}{\hbar} &= J \left(1 - \frac{3(X_A - X_B)}{R} \right) (|r_1 r_2\rangle\langle r_2 r_1| + \text{h.c.}) + \\ &+ \sum_{i,j=1}^2 V_{ij} \left(1 - \frac{6(X_A - X_B)}{R} \right) |r_i r_j\rangle\langle r_i r_j|. \end{aligned} \quad (19)$$

Finally, the last term models the finite lifetimes of the Rydberg states $|r_1\rangle, |r_2\rangle$ via a non-Hermitian Hamiltonian of the form

$$H_{\text{decay}} = -i \sum_{j=1}^2 \frac{\Gamma_j}{2} (|r_j\rangle\langle r_j|_A + |r_j\rangle\langle r_j|_B), \quad (20)$$

where the lifetimes $1/\Gamma_i$ are taken from Ref. [49] and listed in Table II.

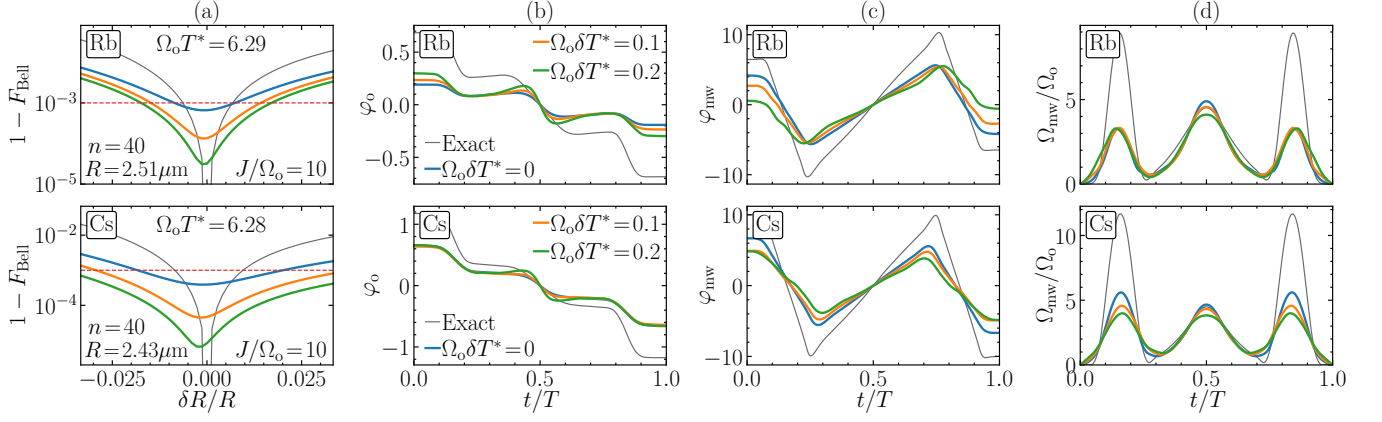


Figure 6. (a) Bell state infidelity as a function of the relative fluctuation in interatomic distance $\delta R/R$. The dark grey line corresponds to the time-optimal exact gate obtained with the procedure outlined in Sec. III B. The colored lines correspond to the robust pulses obtained from the cost function Eq. (16) with $\Omega_o \delta T^* = 0, 0.1, 0.2$, where δT^* is a slight increase of the time-optimal gate time T^* . Here $J/\Omega_o = 10$ and the interaction parameters are in the first row of Table I for rubidium (top) and cesium (bottom) Rydberg states. The horizontal red dashed line is $F_{\text{Bell}} = 0.999$. The control functions are discretized on a time grid of $N = 200$ points, while the integral in Eq. (13) is discretized on $K = 11$ points. The time-optimal pulses for this set of parameters have an execution time $T^* \sim 6.30/\Omega_o$. The pulse shapes for laser phase φ_o , microwave phase φ_{mw} and amplitude Ω_{mw} are plotted in panel (b), (c) and (d), respectively.

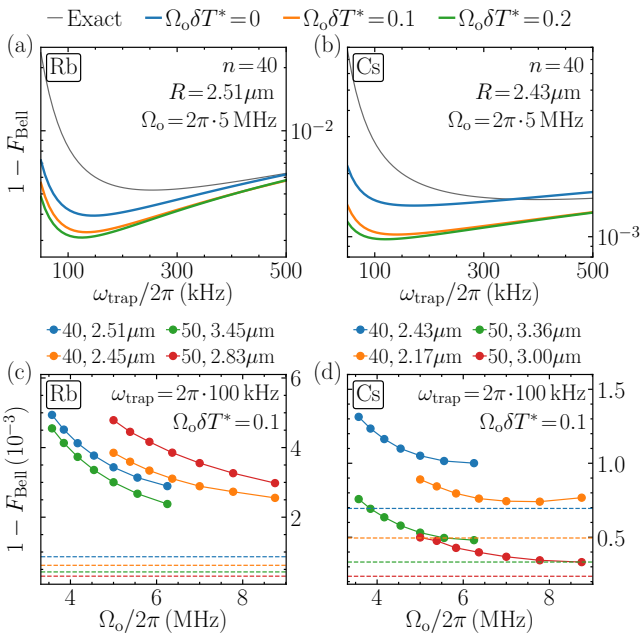


Figure 7. (a)–(b) Bell state infidelity due to atomic motion and Rydberg decay as a function of the trap frequency ω_{trap} for the first row of the interaction parameters in Table I for rubidium (a) and cesium (b). The optical Rabi frequency is $\Omega_o/2\pi = 5$ MHz. The dark grey line and the colored lines correspond to the exact time-optimal protocol and the robust protocols with a time increase δT^* , respectively. (c)–(d) Bell state infidelity as a function of the optical Rabi frequency Ω_o obtained from the robust protocols with $\Omega_o \delta T^* = 0.1$ for all the interaction parameters listed in Table I and a trap frequency $\omega_{\text{trap}}/2\pi = 100$ kHz. The horizontal dashed lines are the infidelities due to Rydberg decay only.

Rb			Cs		
n	$\Gamma_1^{-1}(\mu\text{s})$	$\Gamma_2^{-1}(\mu\text{s})$	n	$\Gamma_1^{-1}(\mu\text{s})$	$\Gamma_2^{-1}(\mu\text{s})$
40	151	60	40	118	69
50	313	126	50	239	141

Table II. Lifetimes for the Rydberg states $|r_1\rangle = |nP_{3/2}\rangle$ and $|r_2\rangle = |nS_{1/2}\rangle$ employed for the numerical simulations presented in Fig. 7 for rubidium (left) and cesium (right) [49].

For the numerical simulations, we set the initial temperature to $2 \mu\text{K}$ and vary the trap frequency between 50 and 500 kHz. We used 8 vibrational modes per atom and verified that this number is sufficient to obtain converged results at all the considered trap frequencies. The results are shown in Fig. 7. We plot the Bell state infidelity as a function of ω_{trap} in Fig. 7(a) and Fig. 7(b) for rubidium and cesium, respectively. The values of J and V_{ij} are taken from the respective first rows of Table I. The dark grey line is the exact protocol, whose execution times are $T_{\text{Rb}}^* \simeq 6.29/\Omega_o$ and $T_{\text{Cs}}^* \simeq 6.28/\Omega_o$, while the colored lines are the robust protocols with $T = T^* + \delta T^*$ (cf. Fig. 6). The latter considerably reduce the gate infidelity, especially at low trap frequencies. Remarkably, there exists an optimal trap frequency that minimizes the infidelity. This non-monotonic behavior is due to the competition between the fluctuating potentials Eq. (19), which worsens the gate performance as ω_{trap} decreases, and the photon recoil Eq. (18), which is known to improve the gate fidelity for decreasing ω_{trap} and for sufficiently small trap frequencies [38]. We note that cesium yields the smallest infidelities thanks to its larger mass, which reduces the oscillator length $x_{\text{osc}} \sim 1/\sqrt{m}$, the larger op-

tical transition wavelength λ_o , which reduces the photon recoil, and the attractive P states van der Waals force (cf. Fig. 6(a)).

In Fig. 7(c) and Fig. 7(d), we plot the gate infidelities obtained from robust protocols with $\Omega_o \delta T^* = 0.1$ for all sets of interaction strengths in Table I and different optical Rabi frequencies $\Omega_o/2\pi \simeq 3.6 - 6.3$ MHz (blue and green markers) and $\Omega_o/2\pi \simeq 5 - 8.75$ MHz (orange and red markers). The total gate times, including the stabilization time δT^* , for such protocols range from $T \simeq 6.44/\Omega_o$ to $T \simeq 6.3/\Omega_o$ for the largest and smallest Rabi frequencies, respectively. The horizontal dashed lines are the fundamental limits set by the Rydberg decay, computed from the exact gate with $T = T^*$ neglecting the atomic motion. Interestingly, while the infidelity for rubidium decreases with increasing Ω_o , it is non-monotonic for cesium, for which an optimal Rabi frequency exists. Moreover, higher n Rydberg states perform slightly worse for Rubidium despite their longer Rydberg lifetime (cf. e.g. orange and red markers in Fig. 7(c)). This is due to the stronger van der Waals interaction $V_{11} > 0$ that makes the gate less robust against atomic motion. On the contrary, for cesium, higher n appears to improve the gate fidelity, implying that larger $|V_{11}|$ with $V_{11} < 0$ is beneficial for stabilizing the gate.

VI. CONCLUSIONS AND OUTLOOK

We showed how resonant dipole-dipole interactions between Rydberg atoms can mediate two-qubit entangling operations. We introduced simple CZ gate protocols that are faster and less sensitive to finite Rydberg lifetimes than the standard schemes based on the van der Waals blockade effect. We generalized our protocol to realistic setups with rubidium and cesium atoms and developed a systematic method to stabilize the gate against fluctuations in the atomic positions, mitigating a main source of fidelity loss. We demonstrated that the stabilized protocols yield Bell state fidelities comparable to or larger than state-of-the-art experimental realizations of neutral-atom entangling gates.

In this work, we only considered experimental implementations with heavy alkali atoms, for which reliable atomic physics calculations can be carried out. Yet, alkaline-earth species such as strontium and ytterbium constitute promising candidates for realizing our scheme, respectively due to the attractive van der Waals interaction between Rydberg states in the singlet series for strontium, and the small predicted C_6 coefficients for states in the single series of ytterbium [50]. Another potential application of the gate protocol outlined in this paper is the realization of long-range gates, thanks to the slower decay with the distance of the resonant dipole-dipole potential with respect to the commonly used van der Waals interaction. Finally, an interesting extension of this work is the generalization of our scheme to multi-qubit gates, which could natively be implemented

on future neutral atom quantum computers.

ACKNOWLEDGMENTS

We acknowledge useful discussions with Sebastian Blatt, Alexander Glätzle, Andreas Kruckenhauser, Matteo Magoni, Cosimo C. Rusconi, Pascal Scholl, and Rick van Bijnen. Giuliano Giudici acknowledges support from the European Union’s Horizon Europe program under the Marie Skłodowska Curie Action TOPORYD (Grant No. 101106005). H.P. acknowledges support by the ERC Starting Starting Grant No. 101041435 (QARA), and the Austrian Science Fund (FWF): COE 1 and quantA. J.Z. acknowledges support from the BMBF through the program “Quantum technologies - from basic research to market” (SNAQC, Grant No. 13N16265), from the Max Planck Society (MPG) the Deutsche Forschungsgemeinschaft (DFG, German Research Foundation) under Germany’s Excellence Strategy—EXC-2111–390814868, from the Munich Quantum Valley initiative as part of the High-Tech Agenda Plus of the Bavarian State Government, and from the BMBF through the programs MUNIQC-Atoms. J.Z. is co-founder and shareholder of PlanQC GmbH. This publication has also received funding under Horizon Europe programme HORIZON-CL4-2022-QUANTUM-02-SGA via the project 101113690 (PASQuans2.1).

Appendix A: Piecewise protocol

As discussed in the main text, the piecewise protocol is composed of two optical π -pulses separated by a slightly-detuned microwave, with $\Delta_{mw} = \mp \Omega_{mw}/\sqrt{3}$, and it yields an exact CZ($\pm 3\pi/2$) gate in the limit of $J/\Omega_o \rightarrow \infty$. The time required is $\Omega_o T = 2\pi + \sqrt{3}\pi \Omega_o/\Omega_{mw}$, which, in the limit of large microwave driving ($\Omega_{mw} \gg \Omega_o$) yields a shorter time than the optimal van der Waals protocol. The time spent in the Rydberg state, however, is slightly less favorable: $\Omega_o T^R = \pi + \sqrt{3}\pi \Omega_o/\Omega_{mw}$. Even in the large microwave driving limit, this is always larger than the van der Waals protocol ($\Omega_o T^R \simeq 2.96$) [26].

We also note that there is an additional solution for $\Delta_{mw} \sim J$, which yields a slightly lower execution time of $\Omega_o T = 2\pi + \sqrt{2}\pi \Omega_o/\Omega_{mw}$. Physically, this detuning brings the state $|r_1 r_2\rangle + |r_2 r_1\rangle$ into resonance with $|r_1 r_1\rangle$, as opposed to the previous case where all dynamics from $|r_1 r_1\rangle$ are trivial (cf. Fig. 2). Similarly to the previous case, no phase modulation is necessary.

While the limit $J/\Omega_o \rightarrow \infty$ is useful for gaining an analytical understanding, it is not the ideal regime for realizing fast gates in a practical setup. For finite interaction strength, we resort to optimal control techniques. Similarly to the main text, we use GRAPE to find an optimal modulation of the detuning $\Delta_{mw}(t)$ for the intermediate pulse. As shown in Fig. 8(a), feasible solutions for each branch are found up to $J/\Omega_{mw} \simeq 2$. The pulses consist of smooth oscillations around their asymptotic

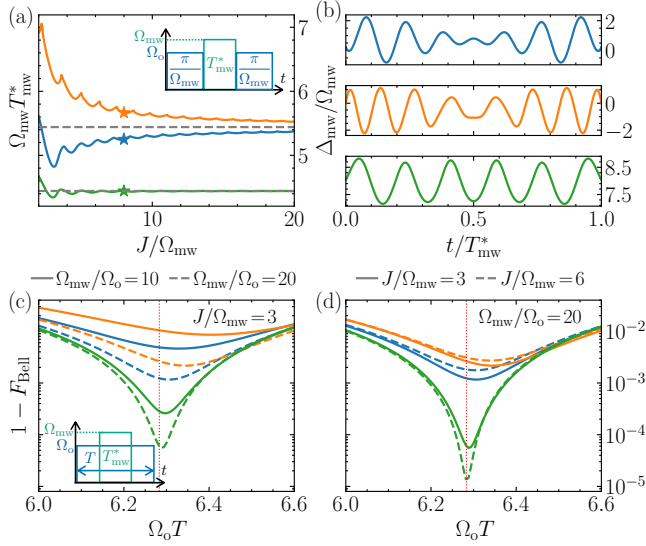


Figure 8. (a) Optimal pulse times for the different branches of solutions for the intermediate pulse in the exact piecewise protocol (see inset). The grey lines correspond to the asymptotic values $\sqrt{2}\pi$ and $\sqrt{3}\pi$. (b) Pulse shape for the different branches of solutions at $J/\Omega_{mw} = 8$ (star). (c)–(d) Bell state fidelity for the approximate piecewise protocol without turning off the laser (see inset). The different branches from (a)–(b) are shown as a function of the duration of the laser pulse $\Omega_o T$, for (c) fixed J/Ω_{mw} and (d) fixed Ω_{mw}/Ω_o . As both parameters are increased, the optimal time T^* approaches $2\pi/\Omega_o$ (red line).

value (cf. Fig. 8(b)), with a frequency increasing with J/Ω_{mw} .

It is worth noting that for large microwave driving, one can still realize an approximate CZ gate without turning off the optical drive during the intermediate pulse. As shown in Figs. 8(c) and 8(d), by using the pulses found previously and simply adjusting the total laser pulse time T , one can achieve the desired gate with a fidelity improving both with Ω_{mw}/Ω_o as well as J/Ω_o . Notably, the branch with $\Delta_{mw} \sim J$ seems to have the highest fidelities compared to the other two. If the regime $J, \Omega_{mw} \gg \Omega_o$ is experimentally accessible, such a piecewise protocol can be appealing for practical implementations as it does not

require any phase modulation on the laser beam.

Appendix B: Finite- V van der Waals protocols

In this section, we briefly discuss gate protocols using only a finite van der Waals interaction. The setup is identical to Ref. [25]. We consider a single Rydberg state $|r\rangle = |r_1\rangle$ for each atom and the laser beam couples it to the computational state $|1\rangle$. The total Hamiltonian is simply

$$\frac{H(t)}{\hbar} = \frac{\Omega_o(t)}{2} \left(e^{i\varphi_o(t)} |1\rangle\langle r|_A + e^{i\varphi_o(t)} |1\rangle\langle r|_B + \text{h.c.} \right) + V |rr\rangle\langle rr|, \quad (\text{B1})$$

Following the analysis of Ref. [25], this Hamiltonian splits into two blocks, each one becoming a two-level system in the limit of V/Ω_o (the so-called blockade limit). This was exploited to perform a pulse optimization using GRAPE, achieving the optimal time of $T \simeq 7.61/\Omega_o$ [26].

Performing a similar optimization for finite V , we obtain several sets of solutions based on the initial condition, as shown in Fig. 9. Remarkably, numerically exact solutions can be found down to the regime of $V \simeq \Omega$. We also note that, contrarily to the asymptotic case, the pulse time does not necessarily correlate with the total time in the Rydberg manifold T^R . Similar pulses have been found in recent works designing Rydberg-dressed gate schemes [51].

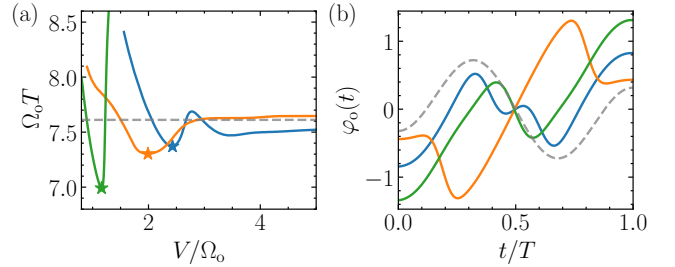


Figure 9. (a) Optimal times for different sets of solutions at finite blockade strength V . The shortest pulse for each branch (highlighted with a star) is shown in (b). The dashed lines correspond to the values in the limit $V/\Omega_o \rightarrow \infty$, previously found in Ref. [26].

-
- [1] H. Bernien, S. Schwartz, A. Keesling, H. Levine, A. Omran, H. Pichler, S. Choi, A. S. Zibrov, M. Endres, M. Greiner, V. Vuletić, and M. D. Lukin, Probing many-body dynamics on a 51-atom quantum simulator, *Nature* **551**, 579 (2017).
- [2] A. Keesling, A. Omran, H. Levine, H. Bernien, H. Pichler, S. Choi, R. Samajdar, S. Schwartz, P. Silvi, S. Sachdev, P. Zoller, M. Endres, M. Greiner, V. Vuletić, and M. D. Lukin, Quantum Kibble–Zurek mechanism and critical

- dynamics on a programmable Rydberg simulator, *Nature* **568**, 207 (2019).
- [3] S. Ebadi, T. T. Wang, H. Levine, A. Keesling, G. Semeghini, A. Omran, D. Bluvstein, R. Samajdar, H. Pichler, W. W. Ho, S. Choi, S. Sachdev, M. Greiner, V. Vuletić, and M. D. Lukin, Quantum phases of matter on a 256-atom programmable quantum simulator, *Nature* **595**, 227 (2021).
- [4] G. Semeghini, H. Levine, A. Keesling, S. Ebadi, T. T.

- Wang, D. Bluvstein, R. Verresen, H. Pichler, M. Kalinowski, R. Samajdar, A. Omran, S. Sachdev, A. Vishwanath, M. Greiner, V. Vuletić, and M. D. Lukin, Probing Topological Spin Liquids on a Programmable Quantum Simulator, *Science* **374**, 1242 (2021).
- [5] R. Tao, M. Ammenwerth, F. Gyger, I. Bloch, and J. Zeiher, High-fidelity detection of large-scale atom arrays in an optical lattice (2024), [arXiv:2309.04717 \[physics.atom-ph\]](https://arxiv.org/abs/2309.04717).
- [6] F. Gyger, M. Ammenwerth, R. Tao, H. Timme, S. Nigirev, I. Bloch, and J. Zeiher, Continuous operation of large-scale atom arrays in optical lattices (2024), [arXiv:2402.04994](https://arxiv.org/abs/2402.04994).
- [7] H. J. Manetsch, G. Nomura, E. Bataille, K. H. Leung, X. Lv, and M. Endres, A tweezer array with 6100 highly coherent atomic qubits (2024), [arXiv:2403.12021 \[quant-ph\]](https://arxiv.org/abs/2403.12021).
- [8] D. Bluvstein, S. J. Evered, A. A. Geim, S. H. Li, H. Zhou, T. Manovitz, S. Ebadi, M. Cain, M. Kalinowski, D. Hangleiter, J. P. Bonilla Ataides, N. Maskara, I. Cong, X. Gao, P. Sales Rodriguez, T. Karolyshyn, G. Semeghini, M. J. Gullans, M. Greiner, V. Vuletić, and M. D. Lukin, Logical quantum processor based on reconfigurable atom arrays, *Nature* **626**, 58 (2024).
- [9] K. Barnes, P. Battaglino, B. J. Bloom, K. Cassella, R. Coxe, N. Crisosto, J. P. King, S. S. Kondov, K. Kotru, S. C. Larsen, J. Lauigan, B. J. Lester, M. McDonald, E. Megidish, S. Narayanaswami, C. Nishiguchi, R. Notermans, L. S. Peng, A. Ryou, T.-Y. Wu, and M. Yarwood, Assembly and Coherent Control of a Register of Nuclear Spin Qubits, *Nature Communications* **13**, 2779 (2022).
- [10] T. M. Graham, L. Phuttitarn, R. Chinnarasu, Y. Song, C. Poole, K. Jooya, A. Scott, P. Eichler, and M. Saffman, Midcircuit Measurements on a Single-Species Neutral Alkali Atom Quantum Processor, *Phys. Rev. X* **13**, 041051 (2023).
- [11] W. Huie, L. Li, N. Chen, X. Hu, Z. Jia, W. K. C. Sun, and J. P. Covey, Repetitive Readout and Real-Time Control of Nuclear Spin Qubits in ^{171}Yb Atoms, *PRX Quantum* **4**, 030337 (2023).
- [12] M. A. Norcia, W. B. Cairncross, K. Barnes, P. Battaglino, A. Brown, M. O. Brown, K. Cassella, C.-A. Chen, R. Coxe, D. Crow, J. Epstein, C. Griger, A. M. W. Jones, H. Kim, J. M. Kindem, J. King, S. S. Kondov, K. Kotru, J. Lauigan, M. Li, M. Lu, E. Megidish, J. Marjanovic, M. McDonald, T. Mittiga, J. A. Muniz, S. Narayanaswami, C. Nishiguchi, R. Notermans, T. Paule, K. A. Pawlak, L. S. Peng, A. Ryou, A. Smull, D. Stack, M. Stone, A. Sucich, M. Urbanek, R. J. M. van de Veerdonk, Z. Vendeiro, T. Wilkason, T.-Y. Wu, X. Xie, X. Zhang, and B. J. Bloom, Midcircuit Qubit Measurement and Rearrangement in a ^{171}Yb Atomic Array, *Phys. Rev. X* **13**, 041034 (2023).
- [13] D. Bluvstein, H. Levine, G. Semeghini, T. T. Wang, S. Ebadi, M. Kalinowski, A. Keesling, N. Maskara, H. Pichler, M. Greiner, V. Vuletić, and M. D. Lukin, A Quantum Processor Based on Coherent Transport of Entangled Atom Arrays, *Nature* **604**, 451 (2022).
- [14] H. Levine, D. Bluvstein, A. Keesling, T. T. Wang, S. Ebadi, G. Semeghini, A. Omran, M. Greiner, V. Vuletić, and M. D. Lukin, Dispersive Optical Systems for Scalable Raman Driving of Hyperfine Qubits, *Physical Review A* **105**, 032618 (2022).
- [15] S. J. Evered, D. Bluvstein, M. Kalinowski, S. Ebadi, T. Manovitz, H. Zhou, S. H. Li, A. A. Geim, T. T. Wang, N. Maskara, H. Levine, G. Semeghini, M. Greiner, V. Vuletić, and M. D. Lukin, High-fidelity parallel entangling gates on a neutral-atom quantum computer, *Nature* **622**, 268 (2023).
- [16] T. M. Graham, Y. Song, J. Scott, C. Poole, L. Phuttitarn, K. Jooya, P. Eichler, X. Jiang, A. Marra, B. Grinkemeyer, M. Kwon, M. Ebert, J. Cherek, M. T. Lichtman, M. Gillette, J. Gilbert, D. Bowman, T. Ballance, C. Campbell, E. D. Dahl, O. Crawford, N. S. Blunt, B. Rogers, T. Noel, and M. Saffman, Multi-Qubit Entanglement and Algorithms on a Neutral-Atom Quantum Computer, *Nature* **604**, 457 (2022).
- [17] G. Unnikrishnan, P. Ilzhöfer, A. Scholz, C. Hölzl, A. Götzelmann, R. K. Gupta, J. Zhao, J. Krauter, S. Weber, N. Makki, H. P. Büchler, T. Pfau, and F. Meinert, Coherent Control of the Fine-Structure Qubit in a Single Alkaline-Earth Atom (2024), [arXiv:2401.10679](https://arxiv.org/abs/2401.10679).
- [18] S. Pucher, V. Klüsener, F. Spriestersbach, J. Geiger, A. Schindewolf, I. Bloch, and S. Blatt, Fine-Structure Qubit Encoded in Metastable Strontium Trapped in an Optical Lattice (2024), [arXiv:2401.11054](https://arxiv.org/abs/2401.11054).
- [19] A. Cao, W. J. Eckner, T. L. Yelin, A. W. Young, S. Jandura, L. Yan, K. Kim, G. Pupillo, J. Ye, N. D. Oppong, and A. M. Kaufman, Multi-Qubit Gates and ‘Schrödinger Cat’ States in an Optical Clock (2024), [arxiv:2402.16289](https://arxiv.org/abs/2402.16289).
- [20] R. Finkelstein, R. B.-S. Tsai, X. Sun, P. Scholl, S. Direkci, T. Gefen, J. Choi, A. L. Shaw, and M. Endres, Universal quantum operations and ancilla-based readout for tweezer clocks (2024), [arXiv:2402.16220](https://arxiv.org/abs/2402.16220).
- [21] S. Ma, A. P. Burgers, G. Liu, J. Wilson, B. Zhang, and J. D. Thompson, Universal Gate Operations on Nuclear Spin Qubits in an Optical Tweezer Array of ^{171}Yb Atoms, *Phys. Rev. X* **12**, 021028 (2022).
- [22] S. Ma, G. Liu, P. Peng, B. Zhang, S. Jandura, J. Claes, A. P. Burgers, G. Pupillo, S. Puri, and J. D. Thompson, High-Fidelity Gates and Mid-Circuit Erasure Conversion in an Atomic Qubit, *Nature* **622**, 279 (2023).
- [23] M. Peper, Y. Li, D. Y. Knapp, M. Bileska, S. Ma, G. Liu, P. Peng, B. Zhang, S. P. Horvath, A. P. Burgers, and J. D. Thompson, Spectroscopy and modeling of ^{171}Yb Rydberg states for high-fidelity two-qubit gates (2024), [arXiv:2406.01482](https://arxiv.org/abs/2406.01482).
- [24] D. Jaksch, J. I. Cirac, P. Zoller, S. L. Rolston, R. Côté, and M. D. Lukin, Fast Quantum Gates for Neutral Atoms, *Phys. Rev. Lett.* **85**, 2208 (2000).
- [25] H. Levine, A. Keesling, G. Semeghini, A. Omran, T. T. Wang, S. Ebadi, H. Bernien, M. Greiner, V. Vuletić, H. Pichler, and M. D. Lukin, Parallel Implementation of High-Fidelity Multiqubit Gates with Neutral Atoms, *Phys. Rev. Lett.* **123**, 170503 (2019).
- [26] S. Jandura and G. Pupillo, Time-Optimal Two- and Three-Qubit Gates for Rydberg Atoms, *Quantum* **6**, 712 (2022).
- [27] C. Fromenteil, D. Bluvstein, and H. Pichler, Protocols for Rydberg Entangling Gates Featuring Robustness against Quasistatic Errors, *PRX Quantum* **4**, 020335 (2023).
- [28] C. Fromenteil, R. Tricarico, F. Cesa, and H. Pichler, Hamilton-Jacobi-Bellman equations for Rydberg-blockade processes (2024), [arXiv:2402.12956 \[quant-ph\]](https://arxiv.org/abs/2402.12956).
- [29] S. Jandura, J. D. Thompson, and G. Pupillo, Optimizing Rydberg Gates for Logical-Qubit Performance, *PRX Quantum* **4**, 020336 (2023).
- [30] L. Henriët, L. Beguin, A. Signoles, T. Lahaye, A. Browaeys, G.-O. Reymond, and C. Jurczak, Quantum Computing with Neutral Atoms, *Quantum* **4**, 327

- (2020).
- [31] D. Yu, H. Wang, D. Ma, X. Zhao, and J. Qian, Adiabatic and high-fidelity quantum gates with hybrid rydberg-rydberg interactions, *Optics Express* **27**, 23080 (2019).
- [32] N. Khaneja, T. Reiss, C. Kehlet, T. Schulte-Herbrüggen, and S. J. Glaser, Optimal control of coupled spin dynamics: design of NMR pulse sequences by gradient ascent algorithms, *Journal of Magnetic Resonance* **172**, 296 (2005).
- [33] A. Garon, S. J. Glaser, and D. Sugny, Time-optimal control of SU(2) quantum operations, *Phys. Rev. A* **88**, 043422 (2013).
- [34] A. Smith, B. E. Anderson, H. Sosa-Martinez, C. A. Riofrío, I. H. Deutsch, and P. S. Jessen, Quantum Control in the Cs $6S_{1/2}$ Ground Manifold Using Radio-Frequency and Microwave Magnetic Fields, *Phys. Rev. Lett.* **111**, 170502 (2013).
- [35] B. E. Anderson, H. Sosa-Martinez, C. A. Riofrío, I. H. Deutsch, and P. S. Jessen, Accurate and Robust Unitary Transformations of a High-Dimensional Quantum System, *Phys. Rev. Lett.* **114**, 240401 (2015).
- [36] B. Riaz, C. Shuang, and S. Qamar, Optimal control methods for quantum gate preparation: a comparative study, *Quantum Information Processing* **18**, 100 (2019).
- [37] P. Scholl, H. J. Williams, G. Bornet, F. Wallner, D. Barredo, L. Henriët, A. Signoles, C. Hainaut, T. Franz, S. Geier, A. Tebben, A. Salzinger, G. Zürn, T. Lahaye, M. Weidemüller, and A. Browaeys, Microwave Engineering of Programmable XXZ Hamiltonians in Arrays of Rydberg Atoms, *PRX Quantum* **3**, 020303 (2022).
- [38] F. Robicheaux, T. M. Graham, and M. Saffman, Photon-recoil and laser-focusing limits to Rydberg gate fidelity, *Phys. Rev. A* **103**, 022424 (2021).
- [39] L. S. Theis, F. Motzoi, F. K. Wilhelm, and M. Saffman, High-fidelity Rydberg-blockade entangling gate using shaped, analytic pulses, *Phys. Rev. A* **94**, 032306 (2016).
- [40] T. M. Graham, M. Kwon, B. Grinkemeyer, Z. Marra, X. Jiang, M. T. Lichtman, Y. Sun, M. Ebert, and M. Saffman, Rydberg-Mediated Entanglement in a Two-Dimensional Neutral Atom Qubit Array, *Phys. Rev. Lett.* **123**, 230501 (2019).
- [41] L. H. Pedersen, N. M. Møller, and K. Mølmer, Fidelity of quantum operations, *Physics Letters A* **367**, 47 (2007).
- [42] P. Virtanen, R. Gommers, T. E. Oliphant, M. Haberland, T. Reddy, D. Cournapeau, E. Burovski, P. Peterson, W. Weckesser, J. Bright, S. J. van der Walt, M. Brett, J. Wilson, K. J. Millman, N. Mayorov, A. R. J. Nelson, E. Jones, R. Kern, E. Larson, C. J. Carey, Í. Polat, Y. Feng, E. W. Moore, J. VanderPlas, D. Laxalde, J. Perktold, R. Cimrman, I. Henriksen, E. A. Quintero, C. R. Harris, A. M. Archibald, A. H. Ribeiro, F. Pedregosa, P. van Mulbregt, and SciPy 1.0 Contributors, SciPy 1.0: Fundamental Algorithms for Scientific Computing in Python, *Nature Methods* **17**, 261 (2020).
- [43] C. S. Adams, J. D. Pritchard, and J. P. Shaffer, Rydberg atom quantum technologies, *Journal of Physics B: Atomic, Molecular and Optical Physics* **53**, 012002 (2019).
- [44] S. Anand, C. E. Bradley, R. White, V. Ramesh, K. Singh, and H. Bernien, A dual-species Rydberg array (2024), [arXiv:2401.10325 \[quant-ph\]](https://arxiv.org/abs/2401.10325).
- [45] G. Bornet, G. Emperauger, C. Chen, F. Machado, S. Chern, L. Leclerc, B. Gély, D. Barredo, T. Lahaye, N. Y. Yao, and A. Browaeys, Enhancing a Many-body Dipolar Rydberg Tweezer Array with Arbitrary Local Controls (2024), [arXiv:2402.11056 \[quant-ph\]](https://arxiv.org/abs/2402.11056).
- [46] S. Weber, C. Tresp, H. Menke, A. Urvoy, O. Firstenberg, H. P. Büchler, and S. Hofferberth, Calculation of Rydberg interaction potentials, *Journal of Physics B: Atomic, Molecular and Optical Physics* **50**, 133001 (2017).
- [47] N. Khaneja, T. Reiss, C. Kehlet, T. Schulte-Herbrüggen, and S. J. Glaser, Optimal control of coupled spin dynamics: design of nmr pulse sequences by gradient ascent algorithms, *Journal of Magnetic Resonance* **172**, 296 (2005).
- [48] R. B.-S. Tsai, X. Sun, A. L. Shaw, R. Finkelstein, and M. Endres, Benchmarking and linear response modeling of high-fidelity rydberg gates (2024), [arXiv:2407.20184](https://arxiv.org/abs/2407.20184).
- [49] I. I. Beterov, I. I. Ryabtsev, D. B. Tretyakov, and V. M. Entin, Quasiclassical calculations of blackbody-radiation-induced depopulation rates and effective lifetimes of Rydberg nS , nP , and nD alkali-metal atoms with $n \leq 80$, *Phys. Rev. A* **79**, 052504 (2009).
- [50] C. L. Vaillant, M. P. A. Jones, and R. M. Potvliege, Long-range Rydberg–Rydberg interactions in calcium, strontium and ytterbium, *Journal of Physics B: Atomic, Molecular and Optical Physics* **45**, 135004 (2012).
- [51] V. Buchemavari, S. Omanakuttan, Y.-Y. Jau, and I. Deutsch, Entangling quantum logic gates in neutral atoms via the microwave-driven spin-flip blockade, *Phys. Rev. A* **109**, 012615 (2024).